

**ARTICLE**

A Novel Starting Impulse Suppression Method for Active Power Filter Based on Slowly Rising Curve

Jianfeng Yang* and Yu Ding

School of Automation and Electrical Engineering, Lanzhou Jiaotong University, Lanzhou, 730070, China

*Corresponding Author: Jianfeng Yang. Email: jfyang@mail.lzjtu.cn

Received: 24 January 2021 Accepted: 08 April 2021

ABSTRACT

With the widespread application of power electronic equipment in the power grid, the harmonic problem of the power grid becomes more pronounced, reducing the efficiency of power production, transmission, and utilization, and interfering with the normal operation of the power grid. Based on the requirements of harmonic suppression and power system protection, a shunt active power filter (SAPF) is proposed as an effective harmonic suppression method. However, there are problems with impulse current and impulse voltage in the starting process of SAPF. Impulse current and impulse voltage cause the power grid and switchgear to bear greater current stress and voltage stress, which seriously affect the security and reliability of the power grid and may damage the switchgear. To effectively solve the problem of impulse current and impulse voltage, the starting process of SAPF is divided into the uncontrolled rectification stage and the transition stage. The mathematical model of the DC side of APF is established. The causes of impulse current and impulse voltage in the uncontrolled rectifier and transition phases are analyzed. By introducing voltage square, a new starting impulse suppression strategy of active power filter based on the slow rising curve is proposed, fundamentally solving the problems of impulse current and impulse voltage. Simulation results verify the effectiveness and feasibility of this method.

KEYWORDS

Shunt active power filter; starting shock; impulse current; impulse voltage

1 Introduction

With the widespread application of high-power electronic devices in recent years, the number of nonlinear electronic devices in the power grid is increasing, leading to an increase in current harmonic pollution in the power grid. Harmonics affect power quality and threaten power system security and stability. Therefore, harmonic control has become a problem to solve in the rapid development of power electronic devices with nonharmonic being a sign of the green and healthy development of power systems [1,2]. The effect and performance of traditional passive power filters cannot meet the current demand, so a parallel active power filter is proposed. SAPF can realize real-time dynamic compensation of harmonics in the power grid, with a good governing effect, fast response speed, and flexible application, and has been widely used in power quality control [3–5].

In the process of grid-connected start-up, SAPF has the problems of DC side voltage overshoot and current surge. Voltage overshoot causes the voltage value on the switch device to exceed the maximum



voltage that the switch device can withstand, resulting in damage to the switch device. Current surge has an impact on the stability and safety of the power grid. Therefore, it is necessary to design a reasonable starting strategy for the SAPF system and the security and stability of the power grid [6–10].

SAPF usually adopts a double closed-loop control mode, with voltage as the outer loop and current as the inner loop. This control mode is simple in structure and easy to realize in the digital system. However, due to the inherent characteristics of Proportion-Integral (PI) Control, there is a deviation between the actual value and the expected value of DC capacitor voltage at the moment of SAPF grid connection. For the controller, the expected value of voltage is equivalent to a step response: the actual value of voltage exceeds the expected value of voltage and results in a certain impulse voltage. The output of the controller in the outer voltage loop is in the form of current value, which further intensifies the current under the control of the inner current loop impact and affects the stability and safety of the system [11–13].

At present, the research on SAPF mainly focuses on the control strategy after stable operation of SAPF. For example, Hekss et al. used cascaded adaptive nonlinear controller based on state space model to solve the problem of photovoltaic system composed of SAPF [14]. Fang et al. proposed an adaptive canvas fuzzy neural network controller based on Fuzzy synovial control to improve the compensation performance of APF [15]. By analyzing the causes of DC bus fluctuation in SAPF under power balance scheme, Meng et al. proposed a feedforward channel method based on cascaded delay signal to reduce DC bus fluctuation and make SAPF better adapt to load change [16]. Al-Gahtani et al. proposed a frequency adaptive control method to deal with the influence of system frequency change on SAPF and ensure its stable operation [17]. Liu et al. proposed an adaptive fractional order synovial control scheme based on RBF neural network to improve the stability and robustness of the system [18]. The above research is mainly to improve the reliability and compensation performance of SAPF after starting, but the research on the starting stage of SAPF is less. Aiming at the current and voltage pulses generated in the start-up phase of SAPF, the causes of the pulses are analyzed, and a method of SAPF start-up pulse based on slow rising curve is designed, which can effectively suppress the current and voltage pulses generated in the start-up phase of SAPF.

The first chapter introduces the background and significance of the research. Chapter two establishes the mathematical model of the DC side SAPF. Chapter three analyzes the causes of the starting shock theoretically. In chapter four, an SAPF starting strategy based on the slow rising curve is proposed. In chapter five, the starting strategy proposed in chapter four is simulated and verified in MATLAB/Simulink. Chapter six summarizes the paper in its entirety.

2 Analysis of Impact Mechanism of SAPF

This paper uses three-phase three-wire SAPF as the research object. The system is mainly composed of a power grid, nonlinear load, and SAPF. The structure diagram is shown in Fig. 1 below. In the figure, e_a , e_b , and e_c are grid voltage; u_a , u_b and u_c are output voltage of three-phase voltage source inverter; i_{La} , i_{Lb} and i_{Lc} are nonlinear load current; i_a , i_b , and i_c are three-phase grid current; i_{ca} , i_{cb} , and i_{cc} are harmonic compensation current of SAPF; R represents equivalent resistance of line, inductance, capacitance and loss of inverter itself; L is filter inductance; C is DC side capacitance; u_{dc} is DC side voltage [19].

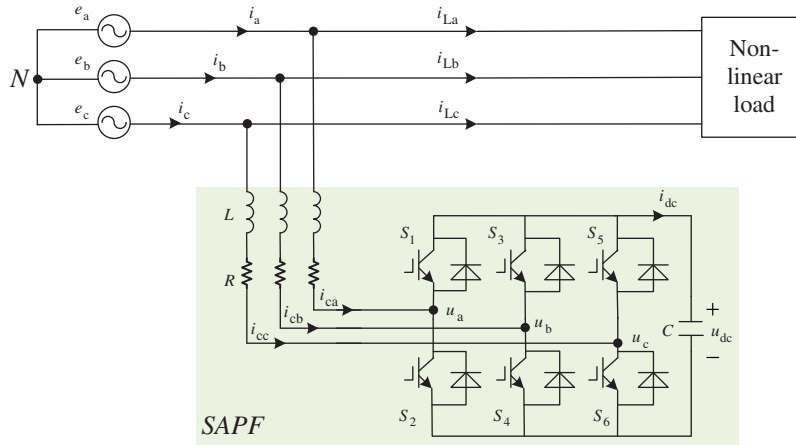


Figure 1: Three-phase three-wire SAPF schematic diagram

According to the SAPF topology in the figure above, it is shown that:

$$\begin{cases} L \frac{di_{ca}}{dt} + Ri_{ca} = e_a - (S_a - \frac{1}{3} \sum_{j=a,b,c} S_j) u_{dc} \\ L \frac{di_{cb}}{dt} + Ri_{cb} = e_b - (S_b - \frac{1}{3} \sum_{j=a,b,c} S_j) u_{dc} \\ L \frac{di_{cc}}{dt} + Ri_{cc} = e_c - (S_c - \frac{1}{3} \sum_{j=a,b,c} S_j) u_{dc} \\ C \frac{du_{dc}}{dt} = S_a i_{ca} + S_b i_{cb} + S_c i_{cc} \end{cases} \quad (1)$$

where S_j is the switching function of the phase bridge arm, $j = a, b, c$.

$$S_j = \begin{cases} 1 & \text{The upper arm is on and the lower arm is off} \\ 0 & \text{The lower arm is on and the upper arm is off} \end{cases} \quad (2)$$

The coordinate transformation of Eq. (1) is carried out, and the three-phase coordinate system is transformed into the two-phase static coordinate system, The SAPF mathematical model under DQ coordinate axis is obtained, as shown in Eq. (3):

$$\begin{cases} L \frac{di_D}{dt} + Ri_{cD} = e_D - S_D u_{dc} \\ L \frac{di_Q}{dt} + Ri_{cQ} = e_Q - S_Q u_{dc} \\ C \frac{du_{dc}}{dt} = \frac{3}{2} (S_D i_D + S_Q i_Q) \end{cases} \quad (3)$$

where S_D and S_Q are switching functions in the two-phase static coordinate system (D, Q).

Eq. (3) is further transformed into an SAPF mathematical model in the two-phase rotating coordinate system (d, q), as shown in Eq. (4):

$$\begin{cases} L \frac{di_{cd}}{dt} + Ri_{cd} - \omega Li_{cq} = e_d - S_d u_{dc} \\ L \frac{di_{cq}}{dt} + Ri_{cq} + \omega Li_{cd} = e_q - S_q u_{dc} \\ C \frac{du_{dc}}{dt} = \frac{3}{2} (S_d i_{cd} + S_q i_{cq}) \end{cases} \quad (4)$$

where S_d and S_q are switching functions in the two-phase stationary coordinate system (d, q). i_{cd} and i_{cq} are dq axis components of the input grid current of SAPF.

In Eq. (4), the

$$C \frac{du_{dc}}{dt} = \frac{3}{2} (S_d i_{cd} + S_q i_{cq})$$

If both sides multiply u_{dc} at the same time, the following Eq. (5) can be obtained:

$$C u_{dc} \frac{du_{dc}}{dt} = \frac{3}{2} (u_d i_{cd} + u_q i_{cq}) \quad (5)$$

The above equation is discretized into:

$$u_{dc}(k) \left[C \frac{u_{dc}(k) - u_{dc}(k-1)}{T_s} \right] = \frac{3}{2} [u_d(k) i_{cd}(k) + u_q(k) i_{cq}(k)] \quad (6)$$

where T_s is the sampling time [20].

In the transition phase, SAPF does not compensate the harmonics of the power grid, so $i_{cq}=0$ can further transform Eqs. (6)–(7):

$$i_{cd}(k) = \frac{2}{3} \frac{u_{dc}(k)}{u_d} \left[C \frac{u_{dc}(k) - u_{dc}(k-1)}{T_s} \right] \quad (7)$$

where u_d is the d-axis component transformed from u_a , u_b , and u_c , which can be obtained by further transforming Eq. (7):

$$i_{cd}(k) = \frac{2}{3u_d} \left[C \frac{u_{dc}^2(k) - u_{dc}(k)u_{dc}(k-1)}{T_s} \right] \quad (8)$$

At this time, for k time, the value of $k-1$ time has been measured, which can be regarded as a constant.

Suppose:

$$M = \frac{2C}{3u_d T_s} \quad (9)$$

$$N = u_{dc}(k-1)$$

By introducing Eq. (9) into Eq. (8), one may get:

$$i_{cd}(k) = M u_{dc}^2(k) - M N u_{dc}(k) \quad (10)$$

The equation above may be obtained:

$$i_{cd}(k) = M \left(u_{dc}(k) - \frac{1}{2}N \right)^2 - \frac{1}{4}N^2 \quad (11)$$

It may be seen from Eq. (11) that $i_{cd}(k)$ is a quadratic function of $u_{dc}(k)$, so the square of DC side voltage value can be controlled as the controlled variable.

3 Analysis of Starting Strategy of SAPF

The start-up of SAPF is divided into two stages: uncontrolled rectifier stage and transition stage.

In the uncontrolled rectifier stage, the DC capacitor voltage can be charged to u'_{dc} by using the reverse diode paralleled by the switch device of the SAPF main circuit.

$$u'_{dc} = 2.34E = \frac{3}{\pi} \int_{\frac{\pi}{3}}^{\frac{2\pi}{3}} \sqrt{6}U_m \sin(\omega t) d(\omega t) \quad (12)$$

where U_m is the effective value of phase voltage.

Taking phase A as an example, when the voltage of phase A reaches the peak value, the SAPF system is put into operation. The maximum impulse current of phase A in the uncontrolled rectification stage is shown in Fig. 2 [21].

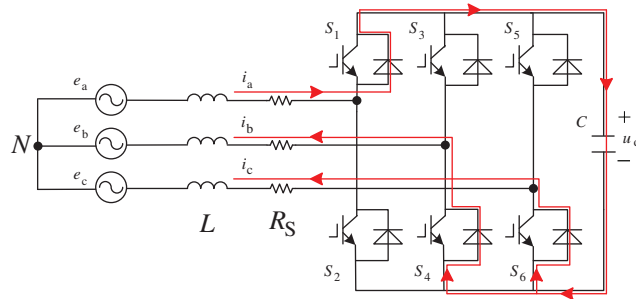


Figure 2: Schematic diagram of grid-connected current at the peak value of phase A

The circuit equation of phase A is as follows Eq. (13):

$$e_a - i_{ca}R_S - L \frac{di_{ca}}{dt} = 0 \quad (13)$$

The grid connection time of phase A is the peak time of a phase:

$$L \frac{di_{ca}}{dt} = 0 \quad (14)$$

According to Eq. (14), Eq. (13) can be simplified to Eq. (15), as shown in Fig. 3.

$$e_a - i_{ca}R_S = 0 \quad (15)$$

Therefore, the starting resistance can be determined by the following equation, where the peak value of and OCP is the level of overcurrent protection (OCP):

$$R_S \geq \frac{P_{e_a}}{OCP} \quad (16)$$

The transition process is the expected value of the DC side voltage when the SAPF works normally when the DC side voltage rises from u'_{dc} . The expected value is set to 800 V in this system.

The SAPF control system adopts double closed-loop control with voltage on the outer loop and current on the inner loop. The outer voltage loop may be expressed as:

$$i_{dc}^* = k_{up}(u_{dc}^* - u_{dc}) + k_{ui} \sum (u_{dc}^* - u_{dc})T_s \quad (17)$$

Among them, u^* dc is the expected value of DC voltage, k_{up} is the proportional gain of the outer loop, and k_{ui} is the integral gain of the outer loop.

The inner current loop is expressed as:

$$u_j = k_{jip}(i_{cj}^* - i_{cj}) + k_{jii} \sum (i_{cj}^* - i_{cj})T_s \quad (18)$$

where i_{cj}^* is the expected current value, k_{jip} is the proportional gain of the inner current loop, and k_{jii} is the integral gain of the inner current loop.

When SAPF enters the transition process of uncontrolled rectification, the expected value of DC side voltage deviates greatly from the actual value. Under the regulation of the PI controller of the voltage outer loop, the output i_{dc} is larger, and the DC side voltage value rises rapidly, causing a certain overshoot and voltage impact. Under further regulation of i_{dc} by the PI controller of the current inner loop, the current i_{cj} rises rapidly and produces a certain overshoot, causing a current impact.

4 Slow Start Strategy

From the previous analysis, we can see that the main causes of SAPF starting impulse are the rapid rise of DC voltage u_{dc} and current i_{cj} in the transition phase. Based on the above reasons, consider limiting the DC side voltage rise speed and current rise speed. Eq. (11) shows that the change rate of the voltage square can affect the current magnitude and current rising speed. Therefore, a rising curve based on the square of voltage can be designed to limit the rate of voltage rise and suppress the impact. Let the rising curve of the transition phase be Y , the transition time be t_s , the expected value of the final DC side be $u_{dc}^* = 800$ V, the DC side voltage at the start of the transition phase is uncontrolled, and the voltage at the end of the rectifier phase is u'_{dc} . Therefore, the rising curve Y can be set as the curve rising from 0 to $U_f = u_{dc}^* - u'_{dc}$.

Fig. 4 shows two traditional rising curves, Y_1 and Y_2 , respectively. Y_2 is a piecewise function composed of Y_{21} and Y_{22} . Eqs. (19) and (20) are their expressions, respectively, and Fig. 3 is the schematic diagram of Y_1 and Y_2 slopes [22,23].

$$Y_1 = \frac{U_f}{t_s} t \quad (19)$$

$$\begin{cases} Y_{21} = 2 \frac{U_f}{t_s} t^2 & 0 < t < t_s/2 \\ Y_{22} = U_f - 2 \frac{U_f}{t_s} (t - t_s)^2 & t_s/2 < t < t_s \end{cases} \quad (20)$$

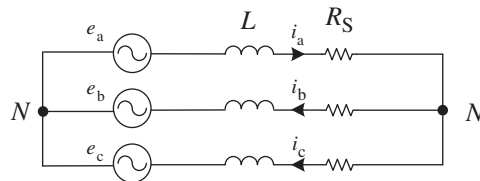


Figure 3: Simplified diagram of grid-connected current at the peak value of phase A

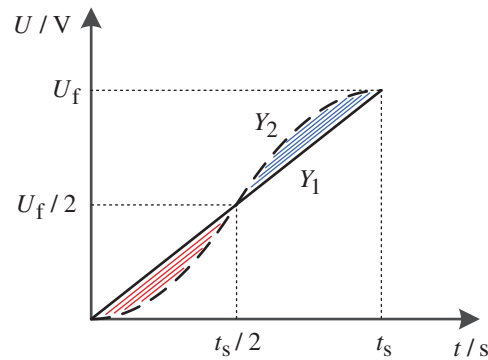


Figure 4: Schematic diagram of the rising curve in two traditional transition stages

It can be seen from Figs. 4, 5, and Eqs. (19) and (20) that the rising curves Y_1 and Y_2 in the transition stage have their advantages and disadvantages. In Eq. (7), Y_1 and Y_2 both improve the step response and restrain the impact to a certain extent. But when Y_1 enters the transition phase, du_{dc}/dt is a certain value and u_{dc} is $2.34E$. According to Eq. (7), a step i_{dc} will be generated, and an impulse current will be generated under the action of PI control in the current inner loop. In the beginning, the instantaneous change rate of Y_2 is 0, but according to Fig. 5, the instantaneous change rate between $t_s/4$ and $3t_s/4$ exceeds Y_1 . According to Eq. (7), the instantaneous change rate will also affect the current. Therefore, there will be a certain current impact.

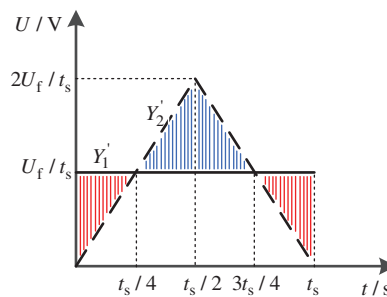


Figure 5: Schematic diagram of the slope of the rising curve in two traditional transition stages

From the above analysis, it may be noted that transition curves Y_1 and Y_2 have their advantages and disadvantages. Therefore, when combining them and taking the advantages of Y_1 and Y_2 to design the transition curve Y_3 as shown in Fig. 6. Y_3 is composed of three parts: Y_{31} , Y_{32} , and Y_{33} . The expression is shown in Eq. (21). The instantaneous change rate of Y_3 is shown in Eq. (22), where $t_2 = t_s - t_1$.

$$\left\{ \begin{array}{l} Y_{31} = \frac{U_f}{2t_1t_2} t^2 \quad 0 < t < t_1 \\ Y_{32} = \frac{U_f}{t_2} t - \frac{U_f t_1}{2t_2} \quad t_1 < t < t_2 \\ Y_{33} = \frac{-U_f}{2t_1t_2} (t - t_s)^2 + U_f \quad t_2 < t < t_s \end{array} \right. \quad (21)$$

$$\left\{ \begin{array}{l} Y'_{31} = \frac{U_f}{t_1 t_2} \quad t_0 < t < t_1 \\ Y'_{32} = \frac{U_f}{t_2} \quad t_1 < t < t_2 \\ Y'_{33} = \frac{-U_f}{t_1 t_2} (t - t_s) \quad t_2 < t < t_s \end{array} \right. \quad (22)$$

Eq. (22) represents the maximum instantaneous rate of change of Y_3 , which is also composed of three parts: Y'_{31} , Y'_{32} and Y'_{33} . The maximum value Y'_3 is determined by t_1 . The smaller the t_1 is, the smaller the starting impact is, which is helpful to restrain the impact, but the t_s is prolonged correspondingly. The schematic diagram of Y'_3 is shown in Fig. 7.

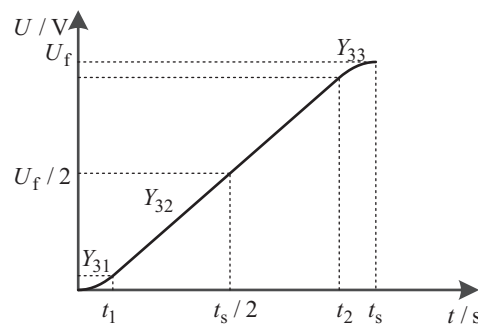


Figure 6: Schematic diagram of rising curve Y_3 in the transition stage

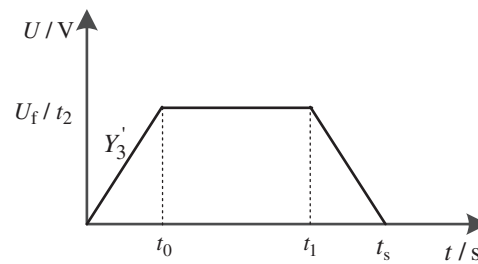


Figure 7: Diagram of instantaneous rate of change Y'_3

However, the transition curve Y_3 still has a disadvantage, that is, i_{dc} will increase with the increase of u_{dc} , which will lead to the gradual increase of impulse current and add instability factors to the system. According to the previous derivation, i_{dc} is related to u_{dc}^2 , so the square of voltage is considered as the outer loop.

Therefore, the final transition phase rising curve combines the advantages of Y_1 and Y_2 and the mathematical relationship between i_{dc} and the design of the improved transition phase rising curve Y_4 as shown in Fig. 8. When the starting time is set to t_0 , the expected voltage rises from $2.34E$. Finally, the transition curve Y_4 is designed as shown in Fig. 7, and the expression is shown in Eq. (23).

$$\left\{ \begin{array}{l} Y_{41} = (2.34E)^2 \quad 0 < t < t_0 \\ Y_{42} = \frac{U_{fn}}{2(t_1 - t_0)(t_2 - t_0)}(t - t_0)^2 \quad t_1 < t < t_2 \\ Y_{43} = \frac{U_{fn}}{(t_2 - t_0)}(t - t_0) - \frac{U_{fn}(t_1 - t_0)}{2(t_2 - t_0)} \quad t_2 < t < t_3 \\ Y_{44} = \frac{-U_{fn}}{2(t_1 - t_0)(t_2 - t_0)}((t - t_0) - t_s)^2 + U_{fn} \quad t_3 < t < t_s \end{array} \right. \quad (23)$$

where

$$U_{fn} = (2.34E + U_f)^2 - (2.34E)^2$$

Because of the square of the introduced voltage, Eq. (13) can be modified to Eq. (24) as follows [20]:

$$\begin{aligned} i_{dc}^* &= k_{up}(u_{dc}^*2 - u_{dc}^2) + k_{ui} \sum (u_{dc}^*2 - u_{dc}^2)T_s \\ &= k_{up}(u_{dc}^* + u_{dc})(u_{dc}^* - u_{dc}) + k_{ui} \sum (u_{dc}^* + u_{dc})(u_{dc}^* - u_{dc})T_s \end{aligned} \quad (24)$$

Let

$$\left\{ \begin{array}{l} k'_{up} = (u_{dc}^* + u_{dc})k_{up} \\ k'_{ui} = (u_{dc}^* + u_{dc})k_{ui} \end{array} \right. \quad (25)$$

By changing the PI parameters, the rising curve based on the square of voltage can be changed back to the traditional rise curve to avoid the huge difference in the square of the voltage.

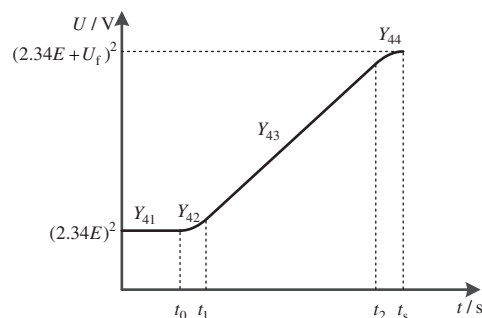


Figure 8: Schematic diagram of rising curve Y_4 in the transition stage

5 Simulation and Verification

To verify the improved transition phase rising curve proposed in this paper, a three-phase three-wire SAPF system model is built in the simulation software. The specific parameters of the system are shown in Tab. 1. The type of nonlinear load is the three-phase uncontrolled rectifier. Fig. 9 shows the nonlinear load current.

Table 1: Simulation model parameters

Parameter	Numerical value
Grid voltage	380 V
Frequency	50 Hz
DC side capacitor voltage	800 V
Inductance	2 mH
Load	5 Ω, 2 mH
Starting resistance	3 Ω

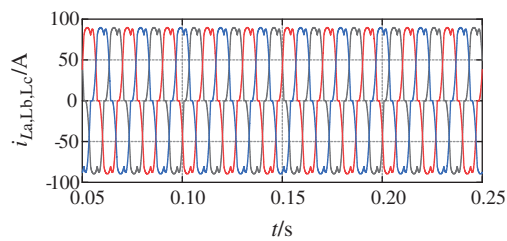


Figure 9: Nonlinear load current

Fig. 10 is the control block diagram of the SAPF system. Before 0.1S, the uncontrolled rectifier boost stage has been completed, and the voltage is stable at $2.34E$. At 0.1S, the switch K_1 is closed, and the system enters the transition stage. During the transition stage, the system does not compensate for the grid harmonics. When the DC side voltage rises steadily to the normal working voltage of 800 V, K_2 is closed, and the system begins to compensate the grid harmonics, and SAPF begins to work. It works normally and the system starts up.

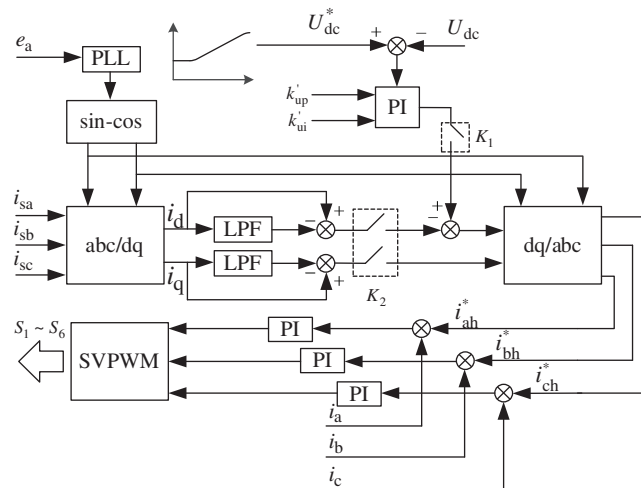


Figure 10: SAPF control block diagram

Fig. 11 shows that the starting strategy is not set, and the expected value of DC side voltage is 800 V. When the 0.1 s system is started, the actual value of DC side voltage is fast-tracking the expected value. The rising rate of DC side voltage is very high, resulting in the current surge as shown in Fig. 11a, and the DC side voltage overshoot, resulting in the voltage surge as shown in Fig. 11b. The impact current is more than four times the normal working current amplitude, and the impact voltage is nearly 200 V higher than the expected working voltage, which seriously threatens the safety of the system.

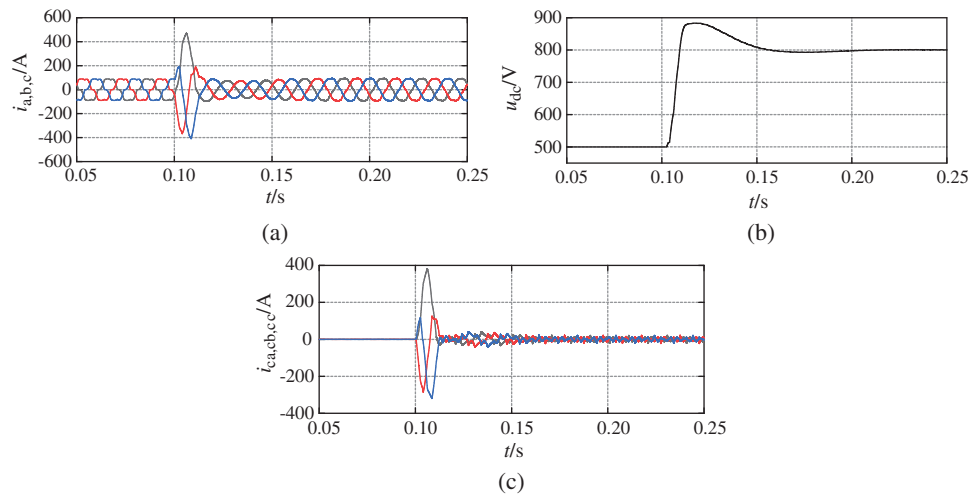


Figure 11: Voltage and current diagram when grid-connected starting strategy is not set. (a) Grid side current (i_a, b, c). (b) DC side capacitor voltage (u_{dc}). (c) SAPF side current ($i_{ca, cb, cc}$)

Fig. 12 shows the voltage and current diagram using the traditional rising curve Y_1 in the transition phase. Compared with Fig. 11, the impulse current and impulse voltage are basically suppressed. However, it can be seen from Figs. 12a and 12c that a large current impulse occurs at the moment when 0.1 s enters the transition phase. At the same time, it can be seen from Fig. 12b that the DC side voltage rises faster at the moment when 0.1 s enters the transition phase. This theoretical analysis is consistent with previous chapters.

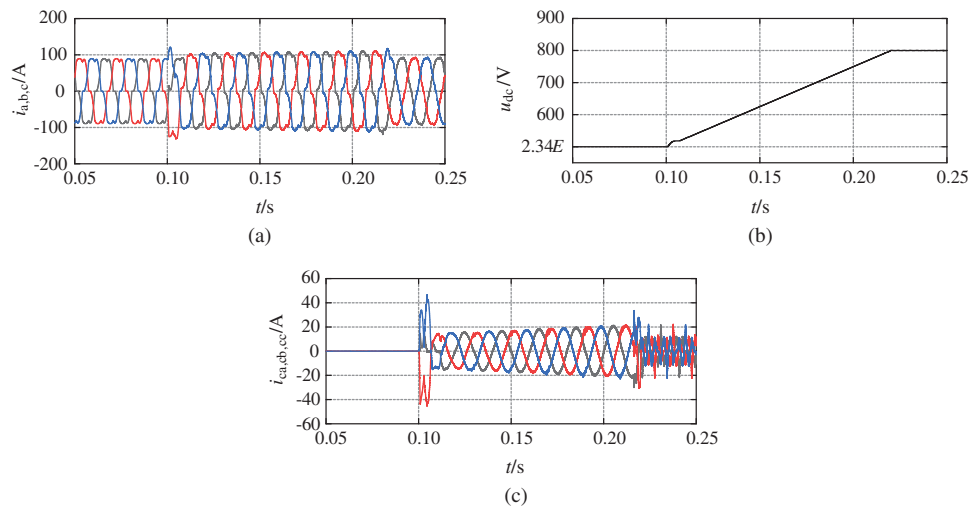


Figure 12: Voltage and current diagram with traditional starting strategy. (a) Grid side current (i_a, b, c). (b) DC side capacitor voltage (u_{dc}). (c) SAPF side current ($i_{ca, cb, cc}$)

Fig. 13 is the voltage and current diagram when the transition phase rise curve Y_3 is adopted. It can be seen from Figs. 13a and 13c that compared with Figs. 12a and 12c, the impulse current entering the transition phase is greatly suppressed, but the current gradually increases during the whole DC side voltage rise process, which increases the instability of the system to a certain extent. It can be seen from Fig. 13b that compared with Fig. 12b, the impulse current entering the transition phase is greatly suppressed. Compared with the whole transition phase, the DC side voltage rises smoothly without overshoot and impact.

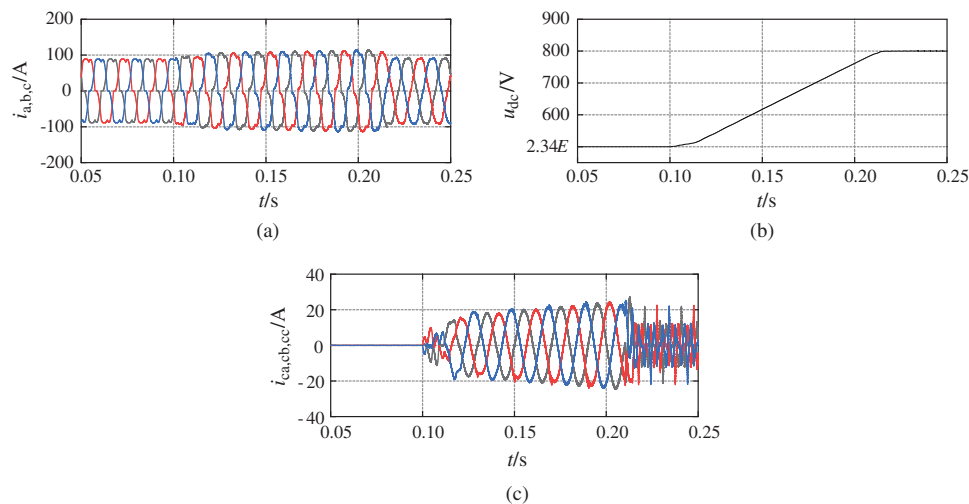


Figure 13: Voltage and current diagram with transition phase rise curve Y_3 . (a) Grid side current (i_a, b, c). (b) DC side capacitor voltage (u_{dc}). (c) SAPF side current ($i_{ca, cb, cc}$)

Fig. 14 shows the voltage and current diagram of the improved transition phase rise curve Y_4 based on voltage square and $t_s=0.12$ s proposed in this paper. It can be seen from Figs. 14a and 14c that compared with Fig. 13, the peak value of current in the whole transition phase is basically consistent, which effectively improves the stability and reliability of the system; during the whole starting process, the DC side voltage rises steadily without overshoot and impact.

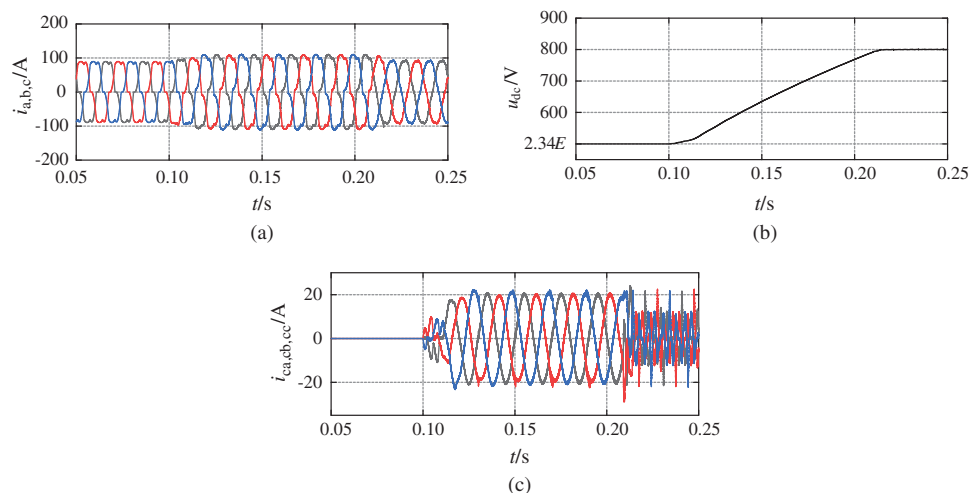


Figure 14: The improved transition phase rise curve Y_4 and $t_s=0.12$ s voltage and current diagram based on voltage square are adopted. (a) Grid side current (i_a, b, c). (b) DC side capacitor voltage (u_{dc}). (c) SAPF side current ($i_{ca, cb, cc}$)

Fig. 15 shows the voltage and current diagram when $t_s = 0.06$ s. Compared with Fig. 14, the starting time is shortened, but the impact is increased, indicating that the greater the starting time is, the better the impact suppression effect is. However, the size of t_s should be determined by comprehensive consideration to suit different systems.

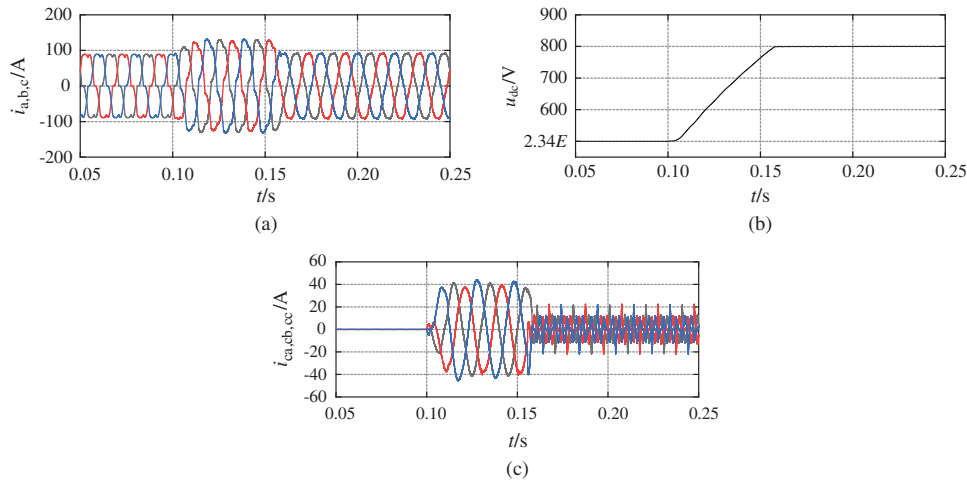


Figure 15: The improved transition phase rise curve Y_4 and $t_s = 0.06$ s voltage and current diagram based on voltage square are adopted. (a) Grid side current (i_a, b, c). (b) DC side capacitor voltage (u_{dc}). (c) SAPF side current ($i_{ca, cb, cc}$)

Fig. 16 shows the change of total harmonic distortion (THD) value before and after the SAPF is put into operation. From the comparison between Figs. 11a and 11b, the THD value is reduced from 24.70% before compensation to 2.92% after compensation, which is in line with the national standard of less than 5%, indicating that the compensation effect of the SAPF system is good.

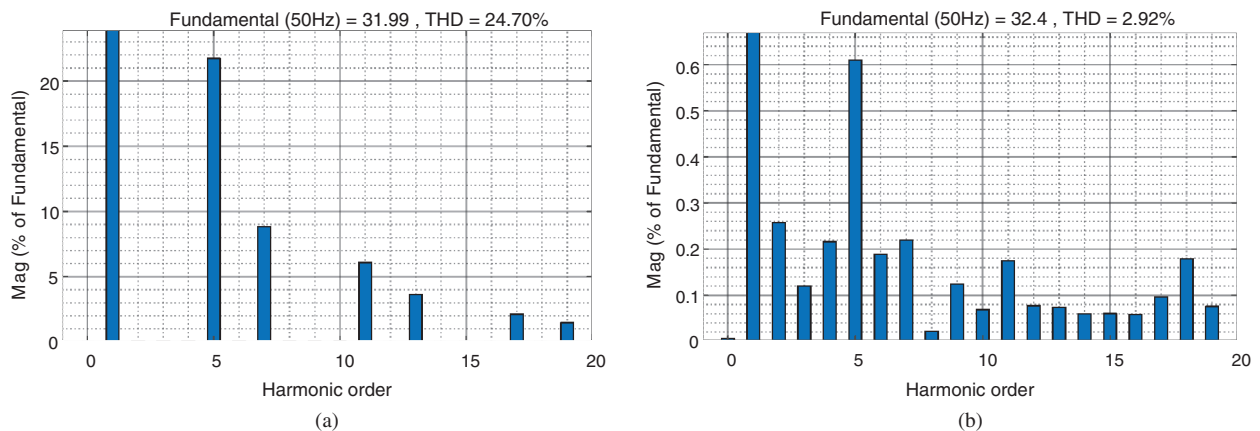


Figure 16: Comparison of THD before and after starting SAPF. (a) Before starting. (b) After starting

6 Conclusion

Aiming at the problem of impulse current and impulse voltage in the process of the grid-connected start-up of the SAPF system, the mathematical model of the DC side of SAPF is established, and the mathematical relationship between AC measured current and DC side voltage is obtained. According to the double

closed-loop PI control system, the causes of impulse are analyzed, and an improved voltage rise curve in the transition phase based on the square of DC side voltage is proposed, which greatly inhibits grid-connected start-up The impact of starting the process. The SAPF system model is built in the simulation software to verify the effectiveness of the transition process rising curve proposed in this paper. Compared with the traditional rising curve, it greatly suppresses the voltage impulse and current impulse at the moment of entering the transition process. Compared with the square rising curve of non DC side voltage, the current of SAPF side will not rise with the rising of DC side voltage, which enhances the security and stability of the system. However, the length of the transition phase, t_s , still needs to be further considered as the next key research direction.

Funding Statement: This work is supported by the National Natural Science Foundation of China under Grant 61863023.

Conflicts of Interest: The authors declare that they have no conflicts of interest to report regarding the present study.

References

1. Li, H., Liu, Y., Yang, J. (2021). A novel FCS-mPC method of multi-level APF is proposed to improve the power quality in renewable energy generation connected to the grid. *Sustainability*, 13(8), 4094. DOI 10.3390/su13084094.
2. Belaidi, R., Haddouche, A., Guendouz, H. (2012). Fuzzy logic controller based three-phase shunt active power filter for compensating harmonics and reactive power under unbalanced mains voltages. *Energy Procedia*, 18(4), 560–570. DOI 10.1016/j.egypro.2012.05.068.
3. Angulo, M., Frasukiewicz, L., Lago, J., Heldwein, M. L., Mussa, S. A. (2013). Active power filter control strategy with implicit closed-loop current control and resonant controller. *IEEE Transactions on Industrial Electronics*, 60(7), 2721–2730. DOI 10.1109/TIE.2012.2196898.
4. Li, G., Zhang, Y., Wang, Y., Sun, Q. (2014). A predictive control based selective harmonic compensation for active power filter. *Power System Technology*, 38(10), 2938–2942. DOI 10.13335/j.1000-3673.pst.2014.10.050.
5. Liu, P., Yang, J. (2019). Research on time-sharing control strategy of shunt APF anti-startup impulse. *2019 3rd International Conference on Electronic Information Technology and Computer Engineering*, pp. 1420–1423. Xiamen, China. IEEE.
6. Tang, Y., Loh, P. C., Wang, P., Choo, F. H., Gao, F. et al. (2011). Generalized design of high performance shunt active power filter with output LCL filter. *IEEE Transactions on Industrial Electronics*, 59(3), 1443–1452. DOI 10.1109/TIE.2011.2167117.
7. Tareen, W. U., Mekhilef, S., Seyedmahmoudian, M., Horan, B. (2017). Active power filter (APF) for mitigation of power quality issues in grid integration of wind and photovoltaic energy conversion system. *Renewable and Sustainable Energy Reviews*, 70, 635–655. DOI 10.1016/j.rser.2016.11.091.
8. Fei, J., Chu, Y., Hou, S. (2017). A backstepping neural global sliding mode control using fuzzy approximator for three-phase active power filter. *IEEE Access*, 5, 16021–16032. DOI 10.1109/ACCESS.2017.2732998.
9. Ouchen, S., Benbouzid, M., Blaabjerg, F. (2020). Direct power control of shunt active power filter using space vector modulation based on super twisting sliding mode control. *IEEE Journal of Emerging and Selected Topics in Power Electronics*. DOI 10.1109/JESTPE.2020.3007900.
10. Senguttuvan, S., Vijayakumar, M. (2018). Solar photovoltaic system interfaced shunt active power filter for enhancement of power quality in three-phase distribution system. *Journal of Circuits, Systems and Computers*, 27(11), 1850166. DOI 10.1142/S0218126618501669.
11. Dash, R., Paikray, P., Swain, S. C. (2017). Active power filter for harmonic mitigation in a distributed power generation system. *2017 Innovations in Power and Advanced Computing Technologies (i-PACT)*, pp. 1–6. IEEE. Vellore, India.

12. Madhu, B. R., Mn, D., Bm, R. (2018). Design of shunt hybrid active power filter (SHAPF) to reduce harmonics in AC side due to non-linear loads. *International Journal of Power Electronics and Drive Systems*, 9(4), 1926. DOI 10.11591/ijpeds.v9.i4.pp1926-1936.
13. Adam, M., Chen, Y., Deng, X. (2018). Harmonic current compensation using active power filter based on model predictive control technology. *Journal of Power Electronics*, 18(6), 1889–1900. DOI 10.6113/JPE.2018.18.6.1889.
14. Hekss, Z., Abouloifa, A., Lachkar, I., Giri, F., Guerrero, J. M. (2021). Nonlinear adaptive control design with average performance analysis for photovoltaic system based on half bridge shunt active power filter. *International Journal of Electrical Power & Energy Systems*, 125, 106478. DOI 10.1016/j.ijepes.2020.106478.
15. Fang, Y., Fei, J., Wang, T. (2020). Adaptive backstepping fuzzy neural controller based on fuzzy sliding mode of active power filter. *IEEE Access*, 8, 96027–96035. DOI 10.1109/Access.6287639.
16. Meng, R., Du, Y., Han, X. (2021). The suppression of DC-link voltage fluctuations through a source active current feedforward in the active power filter. *IET Power Electronics*, 14(2), 481–491. DOI 10.1049/pel2.12001.
17. Al-Gahtani, S. F., Nelms, R. M. (2020). A frequency adaptive control scheme for a three-phase shunt active power filter. *Electrical Engineering*, 103(3), 595–606. DOI 10.1007/s00202-020-01105-4.
18. Liu, N., Fei, J. (2017). Adaptive fractional sliding mode control of active power filter based on dual RBF neural networks. *IEEE Access*, 5, 27590–27598. DOI 10.1109/ACCESS.2017.2774264.
19. Sharma, S., Verma, V., Behera, R. K. (2020). Real-time implementation of shunt active power filter with reduced sensors. *IEEE Transactions on Industry Applications*, 56(2), 1850–1861. DOI 10.1109/TIA.28.
20. Yao, X., Wang, X., Feng, Z. (2016). Research on of improvement of the dynamic ability for PWM rectifier. *Transactions of China Electrotechnical Society*, 31(S1), 169–175. DOI 10.19595/j.cnki.1000-6753.tces.2016.s1.022.
21. Kumar, M., Huber, L., Jovanovic, M. M. (2015). Startup procedure for dsp-controlled three-phase six-switch boost pfc rectifier. *IEEE Transactions on Power Electronics*, 30(8), 4514–4523. DOI 10.1109/TPEL.2014.2351752.
22. Wei, L. (2020). *Research on soft start of thyristors to suppress start-up inrush current of VIENNA rectifier (Master Thesis)*. Chongqing University of Technology, Chongqing.
23. Liu, B., Ben, H., Bai, Y. (2018). A slow given method to suppress the start-up inrush current of PWM rectifier. *Transactions of China Electrotechnical Society*, 33(12), 2758–2766. DOI 10.19595/j.cnki.1000-6753.tces.160517.